metals

Article

A Novel Carbide-Free Bainitic Heavy-Haul Wheel Steel with an Excellent Wear-Resistance under Rolling-Sliding Condition

Tingwei Zhou [1], Haifeng Xu [1], Xinyuan Ma [1], Zhenlin Xu [1], Hai Zhao [1,2] and Yizhu He [1,*]

1 School of Materials Science and Engineering, Anhui University of Technology, Ma'anshan 243002, China
2 Ma'anshan Iron & Steel Co., Ltd., Ma'anshan 243002, China
* Correspondence: heyizhu@ahut.edu.cn

Abstract: With the rapid development of railways towards high speed and larger carrying capacity, the problem of wear and fatigue damage between wheel/rail is gradually becoming serious. However, traditional pearlite wheel/rail has reached the limit, which leads to more attention to developing a novel wheel/rail material. This study aims to report a novel carbide-free bainite wheel steel. The wear-resistance of novel steel was tested by a rolling-sliding wear experiment under heavy-haul condition and investigated the impacts of the running speeds on the damage mechanism of wear and fatigue. The results show that the yield strength of the bainite wheel was as high as 950 MPa and the hardness was 415 HV, which was superior to most of the reported typical wheel steel. During the process of wear, the surface damage of the wheel was mainly adhesive wear and fatigue damage, and the gradient strain layer (GS layer) was formed on the wheel surface. As the running speed increased, fatigue damage gradually became more serious than adhesive wear, and the shear stress and strain of the GS layer were enhanced. The higher thickness and hardening were produced on the GS layer, which is the main reason for the higher wear-resistance of the bainitic wheel under higher running speeds. In addition, the wear-resistance of the novel wheel steel was better than that of the reported wheel steel. This novel bainitic wheel is a promising wheel for heavy-haul condition applications, which could provide a guide in choosing bainitic wheel steel for the railway.

Keywords: heavy-haul trailway; bainitic wheel; wheel-rail wear; hardening; wheel-rail surface damage; running speed

check for updates

Citation: Zhou, T.; Xu, H.; Ma, X.; Xu, Z.; Zhao, H.; He, Y. A Novel Carbide-Free Bainitic Heavy-Haul Wheel Steel with an Excellent Wear-Resistance under Rolling-Sliding Condition. *Metals* **2023**, *13*, 202. https://doi.org/10.3390/met13020202

Academic Editor: Belén Díaz Fernández

Received: 2 December 2022
Revised: 10 January 2023
Accepted: 14 January 2023
Published: 19 January 2023

Copyright: © 2023 by the authors. Licensee MDPI, Basel, Switzerland. This article is an open access article distributed under the terms and conditions of the Creative Commons Attribution (CC BY) license (https://creativecommons.org/licenses/by/4.0/).

1. Introduction

Rolling contact fatigue and wear are the most important ways of causing train wheel-rail failure [1–4], and it not only increases the transportation cost of the railway, but also directly endangers the safety of railways. Therefore, solving the failure problem caused by rolling contact fatigue wear has become the focus of research in the world today. With high-speed passenger lines and heavy-haul rail freight lines, the rolling contact fatigue damage between wheels and rails becomes more and more serious [5,6].

As one of the crucial components of the wheel-rail system, the wheel is required to transmit the force of the wheel–rail interface while carrying the load of the train [7]. The wheel is operated under strong frictional forces and different environmental coupling during rolling contact, and its frictional wear and fatigue damage behavior is bound to be more complex. Thus, the wear and rolling contact fatigue (RCF) resistance of wheel/rail has attracted much scientific interest from researchers. Guo et al. [8] investigated the effects of the slip ratio and contact pressure on the evolution of wear and damage of the CL60 wheel material were explored, which found that the wear and damage of the wheel material are milder under the wet conditions than under the dry conditions. Liu et al. [9] found that pre-wear resulted in an effective strengthening of the wheel surface, which improved the RCF life of wheel specimens under oil lubrication. Faccoli et al. [10] investigated the effect of desert sand on the wear and RCF performance of different wheel steels, which found that sand increased the wear rate of the material, leading to the formation of large cracks on the surface of material. In addition, axle weight and operating speed are also important factors that affect wheel steel RCF damage [11–14]. Ding et al. [15] conducted the effect of running speed on rolling wear and damage behavior of pearlitic wheel rail materials, which found that the wear loss of the wheel roller increased with increasing running speed, and the surface damage morphology of the wheel rollers was dominated by the combination of fatigue cracks and adhesive wear.

In addition to these external conditions, the microstructure of the wheel has a significant effect on the wear and fatigue behavior of the wheel steel [16]. Li et al. [17] found that the fatigue life of lamellar pearlite steel was significantly higher than that of spherical pearlite steel. However, if the alloying elements in the wheel steel are not added in the right proportion during actual manufacturing, the surface of the wheel tread will easily produce a non-uniform microstructure [1,18], which will lead to premature fatigue cracking of the wheel. Zhang et al. [18] found that the non-uniform microstructure consisted of pearlite, pre-eutectoid ferrite and upper bainite. The presence of upper bainite disrupts the continuity and homogeneity of the wheel matrix and produces an uncoordinated plastic deformation with the pearlite, which leads to stress concentration at the interface between the two kinds of microstructure, inducing and promoting the formation of fatigue cracks, further accelerating fatigue wear, and ultimately reducing the wear resistance of the wheel.

According to current smelting technology and material processes, the mechanical strength of traditional pearlite wheel materials has reached a limit, making it difficult to meet the demands of the rapid development of the railway. Therefore, the development of new rail transportation materials has become a hot topic. Compared to pearlitic wheel and rail steels, low-carbon bainitic steels have higher fracture toughness and strength [19–21]. Rezende et al. [22] evaluated the wear resistance and rolling contact fatigue (RCF) of bainitic and pearlitic tissues under dry conditions by double-disk tests, and the results showed that bainitic tissues possess better wear resistance and fatigue resistance than pearlitic tissues; Miranda et al. [23] found that the bainitic microstructure was more resistant to crack extension than pearlite, resulting in less mass loss. In addition, rails made of bainitic steels have a longer contact fatigue life than pearlitic steels [24–26]. Therefore, bainitic steel is considered a potential alternative to pearlitic wheel rail steel. Recently, the effect of microstructure on mechanical properties of bainitic steel have attracted much attention [23,27,28]. The obtained results revealed that the heat treatment progress plays an essential role in determining the microstructure of bainitic steels. Valizadeh et al. [29] revealed that the volume percent of retained austenite in bainitic steel decreases with decreasing the isothermal transformation temperature. The fraction of blocky austenite in the microstructure is largely suppressed by choosing particular chemical composition of the steel and low isothermal transformation temperature to maximize the bainite fraction [30]. During isothermal transformation, the austenite transforms to bainitic ferrite and thin film-like retained austenite, which between bainitic laths are more stable than large blocky austenite because of higher C concentration and transformation constraints exerted by the surrounding ferrite [31]. Xu et al. [32] emphasized the ratchetting is performed on the carbide-free bainitic (CFB) rail steel by low-cycle fatigue experiments under different heat-treatment conditions. They found that online controlled cooling could enhance the fatigue resistance of CFB steel more than air cooling. Moreover, bainitic steels with a lower transformation temperature showed a greater wear resistance [33]. To meet the increasing industrial demands, the service condition of the railways becomes more severe, such as higher running speed and larger capacity. Those severe service conditions will cause the acceleration of fatigue and wear damage for a wheel material, consequently leading to the expressive decline of the service life of wheel/rail materials. The pearlitic wheels have been widely used in heavy-haul railways systems all over the world. However, they have suffered from damage with different degrees under various working conditions during the harsh service conditions. The wear rate of pearlitic materials increases with increasing axle load [7] and running speed [15], but decreases with the increase of curve radius. While there are many studies on the damage behavior of wheel materials under harsh conditions, which provide valuable insights, extending the service life of wheel materials remains a challenge. Given the fact that bainitic steel is considered a potential alternative to pearlitic wheel/rail steel, the failure mechanism of bainitic wheel materials under harsh conditions has not been studied in great detail yet.

In view of the outstanding issue discussed above, the present work aims to extend the knowledge of the effect of running speed on the wear resistance and fatigue resistance of bainitic wheel steels. The wear and fatigue damage behavior of bainitic wheel steels was analyzed by wear rate, hardening rate, surface abrasion, fatigue cracking and plastic deformation of wheel specimens. This paper tends to provide a theoretical basis for exploring the mechanism of damage of new bainitic wheels, optimizing wheel materials, and improving the safety of trains in service.

2. Materials and Methods

2.1. Test Steel

The specimens used in the rolling-sliding wear experiment were two types of materials. The main specimen was taken from a novel bainitic wheel steel (BW), and the accompanying specimen was taken from a pearlitic rail steel (U75V, 310 HV, Chinese standard: GB/T 2585-2007). As illustrated in Figure 1a, the heat treatment process of the wheel steel consists of two main stages: Austenitizing and tempering. The specimens were heated to the austenitization temperature (900~920 °C) with a heating rate of 10 °C/s and held for 30 min under a vacuum. Afterwards, specimens were cooled (cooling rate: 5 °C/s) to room temperature and tempered for 2 h. Bainitic transformation occurred during continuous cooling. The cooling rate was enough to avoid the formation of other phases which exist prior to bainite transformation according to the CCT diagram (Figure 1b). The chemical composition of the wheel steel is listed in Table 1. To provide insight into the yield strength and hardness of the novel BW presented in this study, which were listed in Table 2, alongside some representative wheel steel reported in previous studies (Table 3). The yield strength and microhardness value of the BW are higher than those of most of the typical wheel steels from American, Chinese, and European Standards.

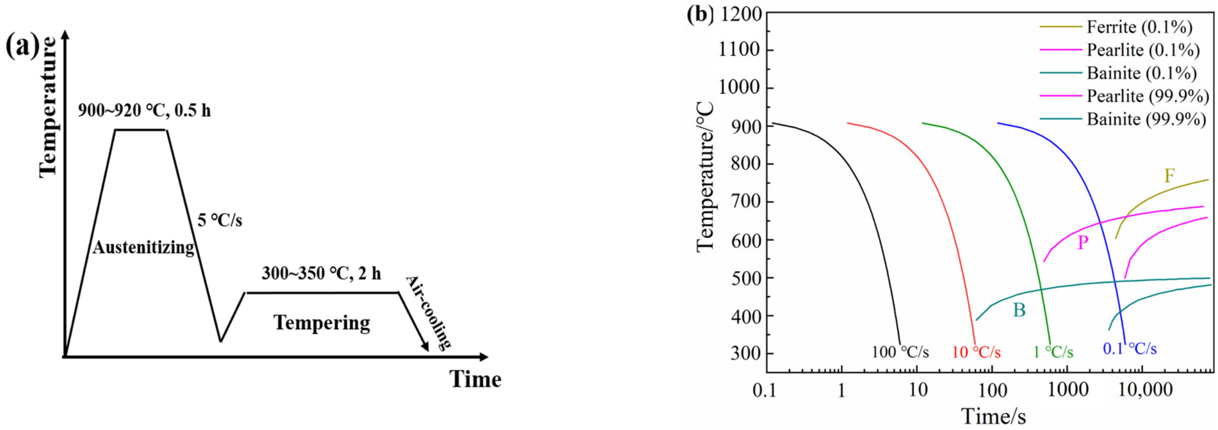

Figure 1. (**a**) The thermal treatment process of the test steel, and (**b**) calculated CCT diagram of the test steel using JMat-Pro.

Table 1. Chemical composition (wt%) of the test steel.

C	Si	Mn	Cr	Ni	Mo	Cu	V
0.22~0.24	1.53~1.55	2.04~2.06	0.04~0.06	0.38~0.40	0.34~0.36	0.26~0.30	0.06~0.08

Table 2. Mechanical properties of the test steel.

Yield Strength/MPa	Tensile Strength/MPa	Elongation/%	Microhardness/HV
960 ± 15	1050 ± 20	18 ± 2	415 ± 10

Table 3. Hardness, chemical composition (wt%) and yield strength of the representative wheel materials reported in previous studies.

Material	C	Si	Mn	Hardness/HV	Yield Strength/MPa	Ref.
1. CL60	0.55~0.65	0.17~0.37	0.50~0.80	277	580	[34]
2. CL65	0.57~0.67	≤1.00	≤1.20	302	620	[34]
3. CL70	0.67~0.77	≤1.00	≤1.20	321	650	[34]
4. Class B	0.65	0.63	0.26	330	642	[35]
5. Class B+	0.63	0.84	0.88	340	690	[35]
6. ER7	0.51	0.78	0.38	295	568	[35]
7. ER8	0.52	0.26	0.73	285	610	[36]
8. D2	0.50~0.56	0.90~1.10	0.90~1.10	270	570	[37]

Figure 2 shows that the microstructure of the wheel steel, which consists of carbon-enriched retained austenite (film-like) embedded in exceptionally fine plates of carbide-free bainitic ferrite, as the precipitation of carbides is suppressed by the high silicon content (more than 1.5 wt%).

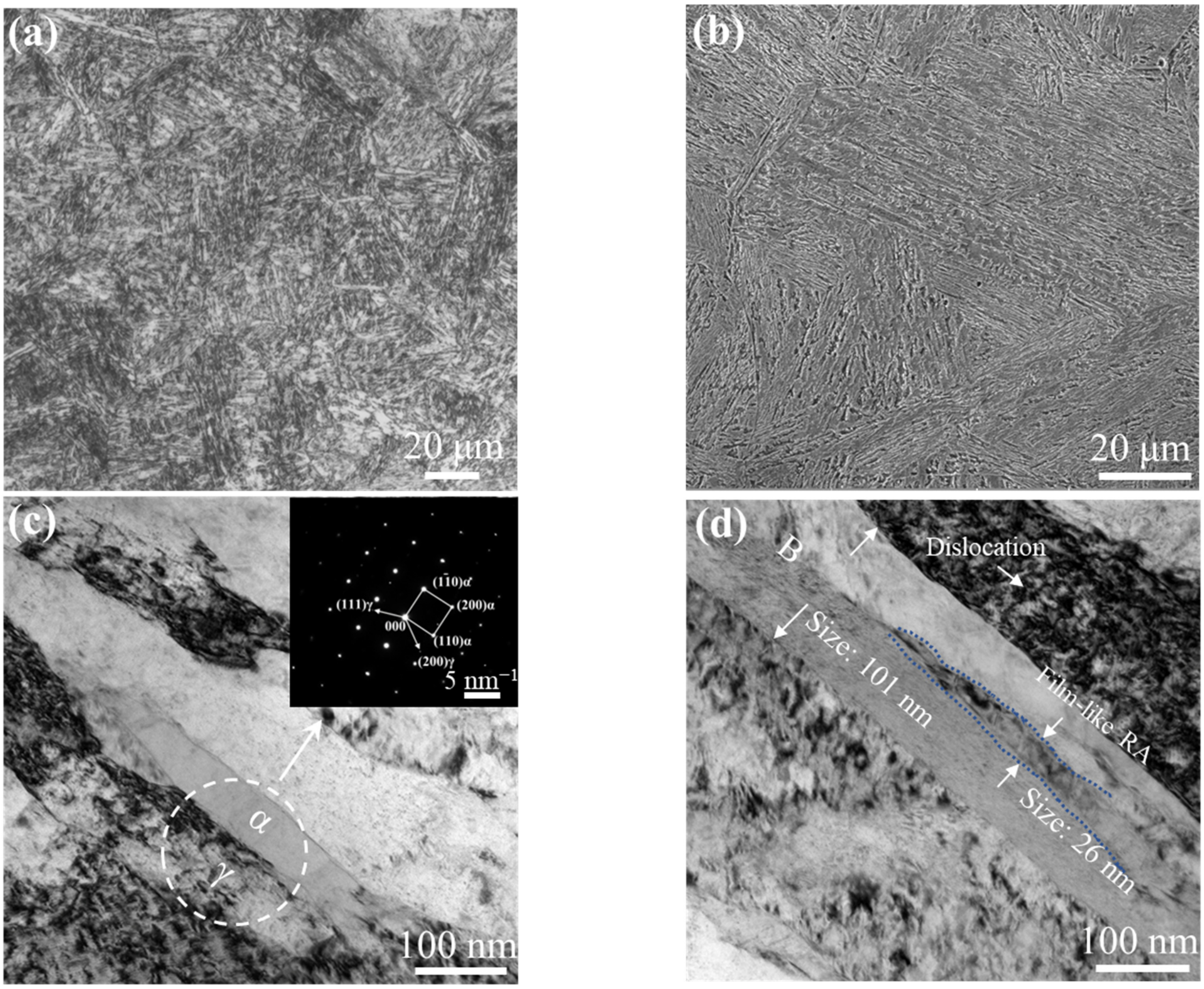

Figure 2. The original microstructures of the wheel specimens: (**a**) OM image; (**b**) SEM image; (**c**,**d**) TEM image.

2.2. Microstructural Characterization

The microstructure of the specimens was characterized by optical microscope (OM, ZEISS Axiovert 40MAT, Oberkochen, Germany), field-emission scanning electron microscope (FESEM, Tescan MIRA3 XMU, Brno, Czech Republic), and transmission electron microscope (TEM; Tecnai G2 F20 S-TWIN, Hillsboro, OR, USA). Specimens for FESEM were prepared by mechanical polishing and then etched with 4% nitric acid alcohol. The cross-section of samples for microstructure observation was perpendicular to the wear surface and parallel to the rolling direction.

2.3. Dry Rolling–Sliding Wear Test

The rolling–sliding tests were performed on a twin-disc wear testing machine (Wear Tester, CQHH-RCF-1, Chongqing, China), which was previously used in wheel–rail contact studies under dry conditions. The test specimens were cylindrical rings with Ø60 mm outer diameter, Ø30 mm inner diameter and 20 mm thickness. The contact width between the two discs was 5 mm. The upper one machined from the wheel steel and the lower one machined from the standard rail steel. The schematic diagram of the tester is shown in Figure 3. The maximum contact stress between the two samples in point contact mode was calculated using Hertz contact theory and simulation criteria. The method is shown in Equation (1) [38]:

$$\sigma_{max} = \frac{852.6}{\alpha \cdot \beta} \times \sqrt[3]{F(\Sigma\rho)^2} \tag{1}$$

where ρ is the curvature at the contact point between the twin disc determined by the sample radius size (unit: mm^{-1}). σ_{max} is the maximum contact stress (unit: MPa). α and β are point contact deformation coefficients determined by the auxiliary parameter $cos\tau$, obtained from YB/T 5345-2014 standard [39]. F is the vertical load applied to the sample (unit: N). The operation condition of a heavy-haul train with the axle load of 35 t and the wheel diameter of 840 mm was simulated. The maximum contact stress simulated in the experiment between the wheel and rail was 1200 MPa. According to Equation (1), the pressure load was calculated to be 3035 N. The actual angular velocity of wheels (ω) could be calculated with the following formula:

$$\omega_{wheel} = \frac{V}{R} \tag{2}$$

where ω_{wheel} is the actual angular velocity of wheels, V represented the actual operation speed of heavy-haul trains (80, 120, 150 km/h), and R represented the radius of wheels. Therefore, the experimental rotational speed could be calculated in the following way:

$$N_{exp} = N_{wheel} = \frac{\omega_{wheel}}{2\pi} \tag{3}$$

where N_{exp} is the experimental rotational speed of wheels, and N_{wheel} is the actual rotational speed of wheels.

From Formula (3), the rotational speeds were 546, 740, and 950 $r{\cdot}\mathrm{min}^{-1}$, and the rolling cycles were 30,000. The slippage ratio of wheel/rail specimens was about 10%. All experiments were conducted at room temperature. The main test parameters are shown in Table 4.

Table 4. Test parameters and calculation results of contact stress.

Running Speed/km·h^{-1}	Rotational Speed/r·min^{-1}	Vertical Load/N	Slip Rate/%	Number of Cycles
80	546	3035	10	30,000
120	740	3035	10	30,000
150	950	3035	10	30,000

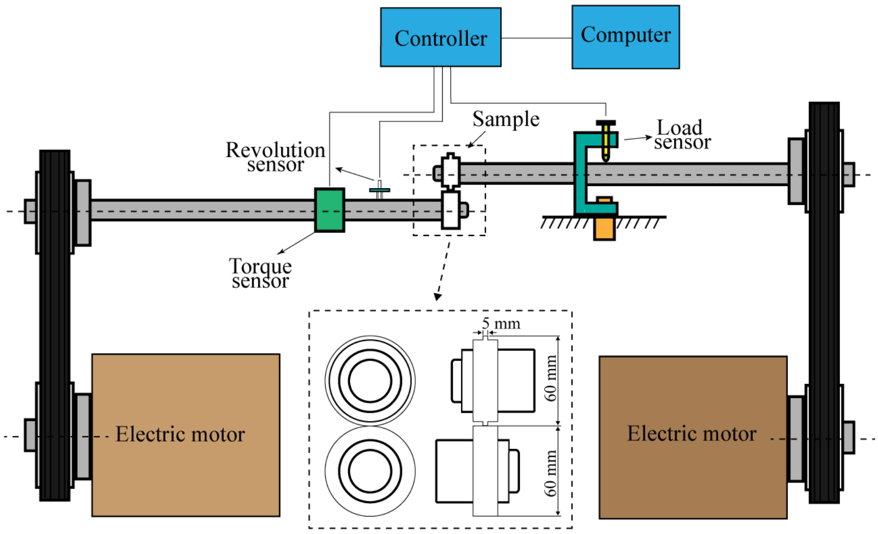

Figure 3. Experimental setup for the rolling-sliding tester.

3. Results

3.1. Wear Resistance

The specific wear rate (*SWR*) is the volume loss per unit load and the distance traveled by a point on the perimeter during the wear test.

$$SWR = \frac{V}{F_N \times S_d} \tag{4}$$

where V is volume loss, S_d is wearing distance, and F_N is load.

Figure 4 shows the wear loss of the wheel specimens with increasing running speed. The mass loss of wheel roller under higher rotational speed (80 km/h) is higher than that under lower speed (150 km/h), with the similar trend of the *SWR*. Therefore, it is clear that the wear loss of the wheel declines with the increase in running speed.

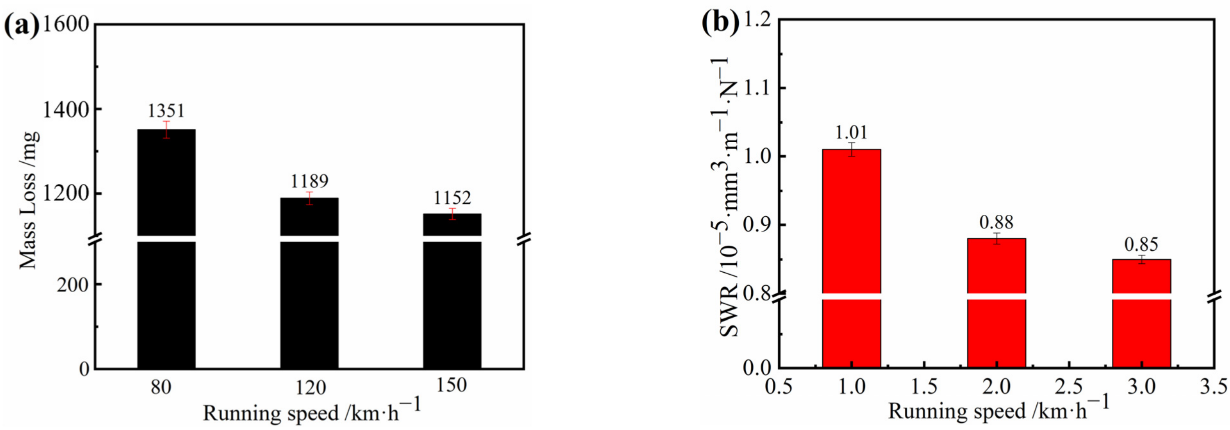

Figure 4. Wear loss of the wheel specimens with increasing running speed: (**a**) Mass loss and (**b**) specific wear rate.

3.2. The Morphology of Wear Surface

Figure 5 shows the microscopic morphology of the wear surface of the specimens at different speeds. It can be seen that the surface of the wheel specimen is dominated by adhesive wear and fatigue cracks. The cracks, delamination and peeling off of the specimen surface were observed at the low speed (80 km/h) (Figure 5(a1,a2)). Cracks are caused by cyclic stresses expanding towards the interior of the matrix and folding back towards the surface, in which cases spalling to form severe peeled blocks [7]. In addition, a small number of pits were found on the surface of the specimen, the wear mechanism of this surface specimen is not only fatigue wear and adhesive wear, but also a small amount of pitting fatigue flaking when the degree of wear is serious. As the speed increases, the surface of specimen became more densely packed with pitting pits and a large number of pockmarks appeared, indicating that the wear mechanism of specimen changes to a mainly pitting fatigue spalling at 120 km/h, where the wear was reduced, but the fatigue damage was increased (Figure 5(b1,b2)). Finally, almost no pitting pits were observed on the specimen surface at 150 km/h, and there is a large amount of flattened puckering (Figure 5(c1,c2)), which indicated that the specimen surface was dominated by fatigue wear.

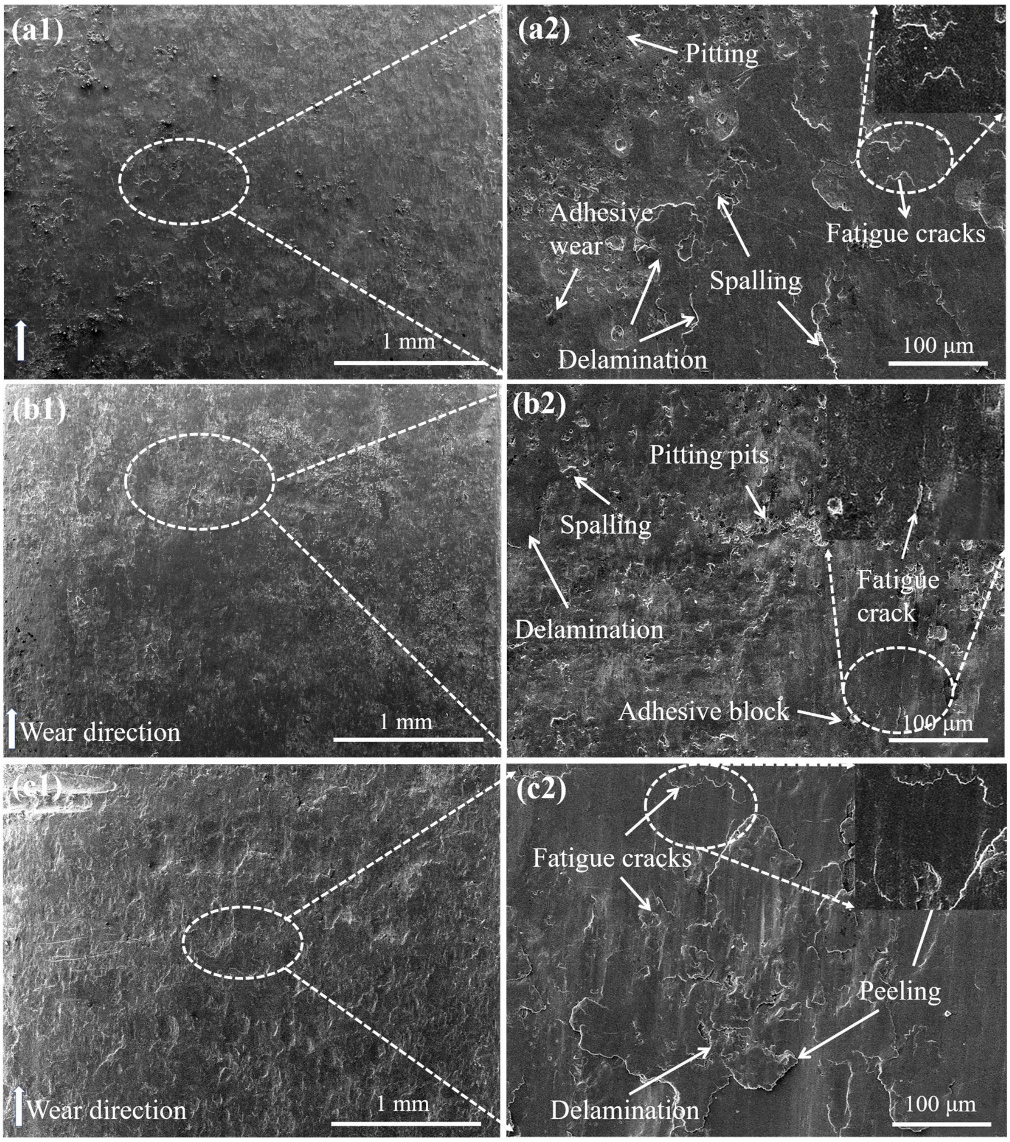

Figure 5. FESEM images of the wear surface of the test steel: (**a1**,**a2**) 80 km/h, (**b1**,**b2**) 120 km/h and (**c1**,**c2**) 150 km/h.

3.3. Microstructure of the Gradient Strain Layer

Plastic deformation of the material occurs under cyclical load, which gradually accumulates and eventually forms a gradient strain layer on the wheel surface due to the ratchet effect [10,40,41]. Figure 6 shows the original morphology of plastic deformation in the cross-section of the specimens. After the wear test, a gradient strain layer (GS layer) was formed on the surface of the specimen. As the speed increased, the plastic deformation of the wheel became more severe. With the running speeds increasing from 80 km/h to 150 km/h, the thickness of the GS layer (T_{GS}) increased from 42 μm to 110 μm.

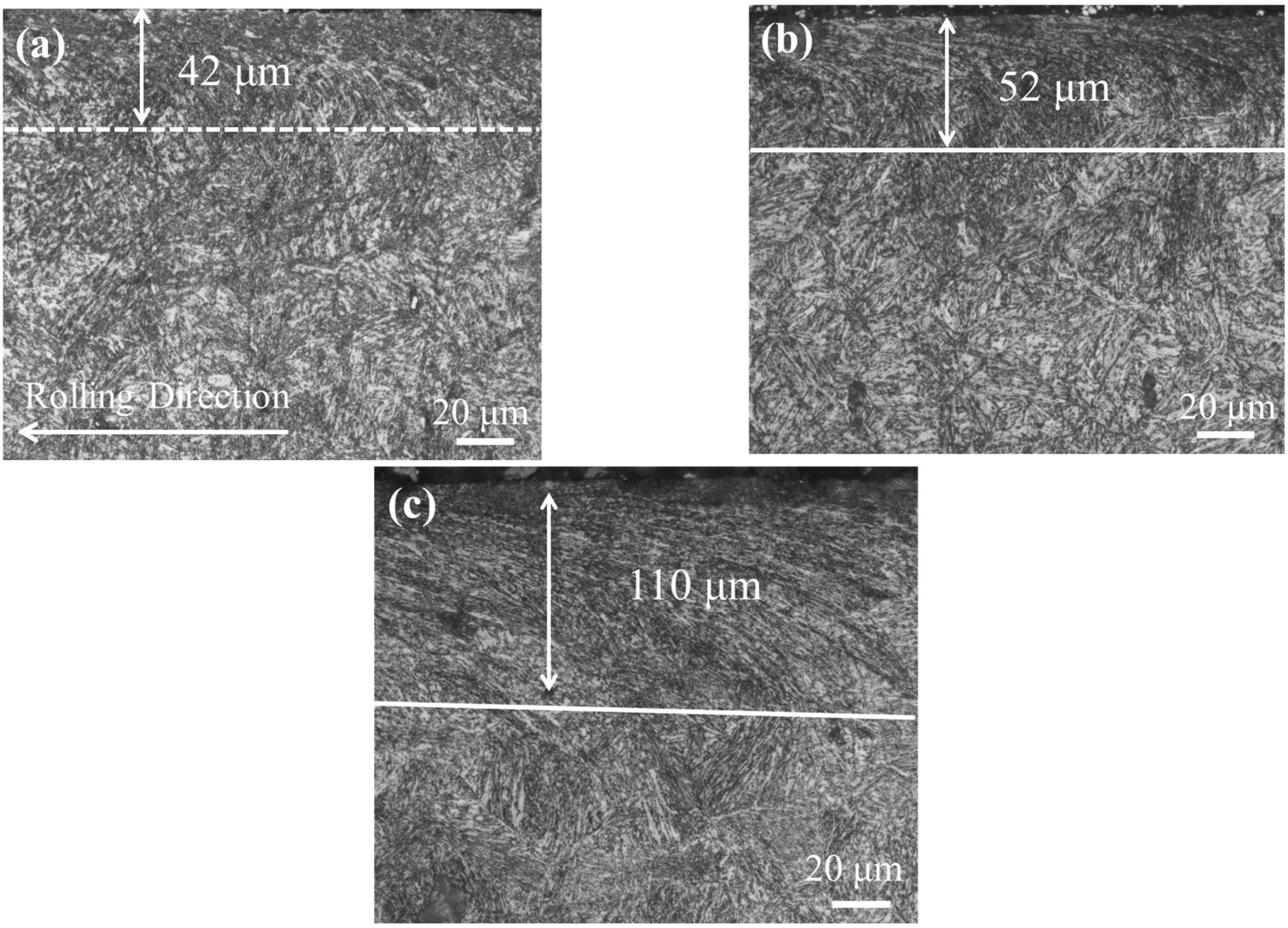

Figure 6. OM images of the gradient strain layer of the wheel specimens: (**a**) 80 km/h, (**b**) 120 km/h and (**c**) 150 km/h.

In order to further investigate the microstructure evolution of the wheel steel, the surface of the specimens can be divided into three zones, as shown in Figure 7. As shown in the above results, the topmost surface of the specimens was the severe plastic deformation (SPD) zone with the deepest bainite refinement, almost parallel to the surface of the specimens (Figure 7a (I)). The light plastic deformation (LPD) zone was closed to the matrix, with shallow plastic deformation and curved bainite flow lines, while the direction of the bainite slats in the matrix region was randomly arranged (Figure 7a (II)). Thus, the degree of bainite lath and the refined grain size gradually increase from the matrix to the topmost surface. Further observation of the topmost surface layer (SPD zone) showed that the bainite was extruded and fragmented into submicron grains and thin lath. The degree of grain refinement and grain size in the topmost surface layer of the wheel specimens were similar for different rotational speed conditions (Figure 7(a1,b1,c1)).

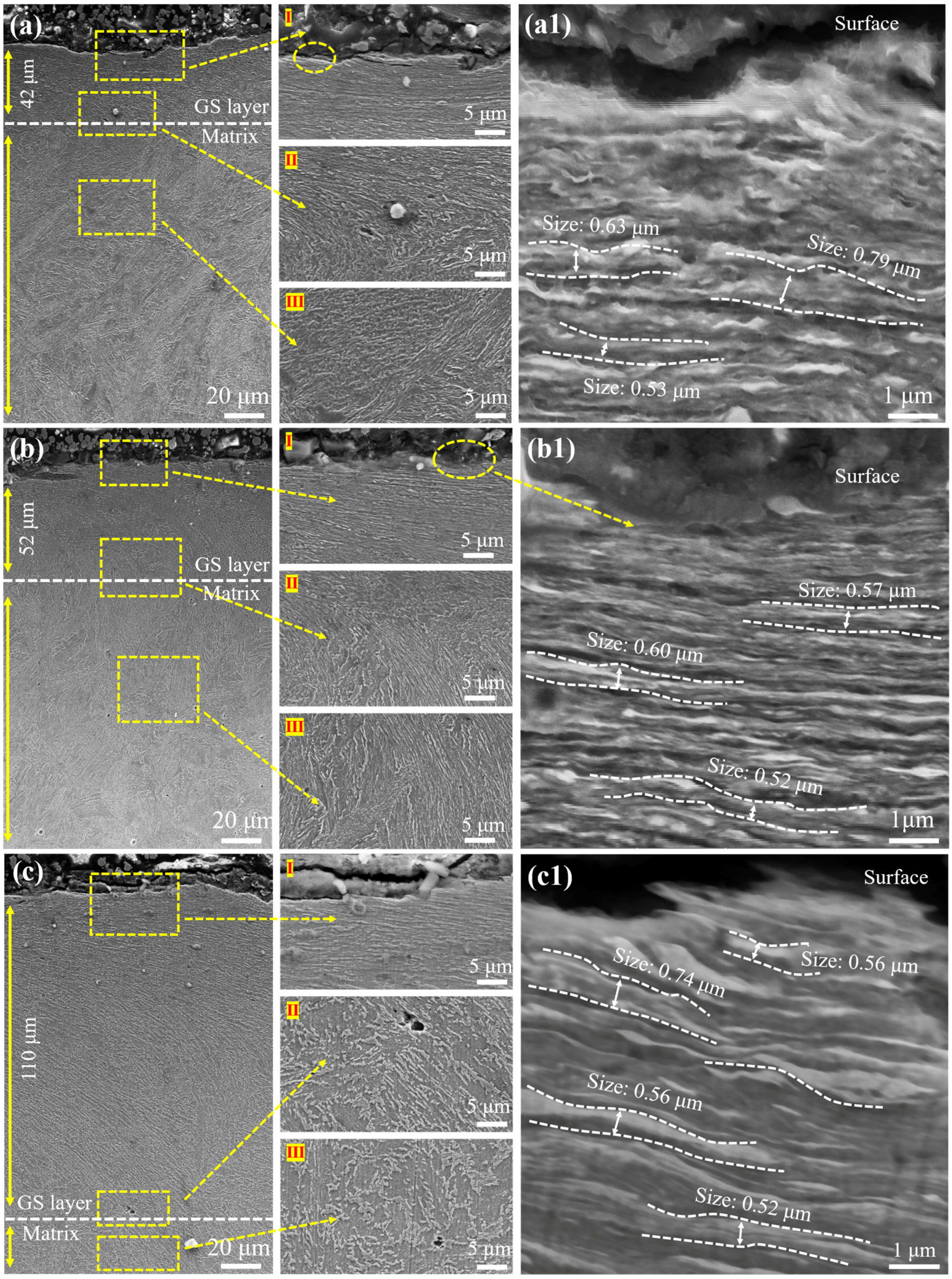

Figure 7. FESEM images of the gradient strain layer of the test steel: (**a**,**a1**) 80 km/h, (**b**,**b1**) 120 km/h and (**c**,**c1**) 150 km/h.

3.4. The Distribution of Shear Strain and Hardness

The materials on the contact surfaces are subjected to positive and shear stresses [42], which will lead to a rheological structure. The degree of bending of the bainite can often be used to reflect the intensity of plastic deformation [43]. The shear strain can be calculated by the displacement field of the plastic flow line, which will reflect the degrees of the bending of bainitic lath, as shown in Figure 8a. The calculation equation of equivalent shear strain is as follows [44]:

$$\varepsilon = \frac{\tan(\theta)}{\sqrt{3}} \tag{5}$$

where θ is the angle of shear at different depths on the plastic flow line, ε is the equivalent shear strain, and $tan(\theta)$ is the slope of the tangent line of the rheological curve.

$$y(x) = y_0 + A \times \exp^{Rx} \tag{6}$$

where $y(x)$ is the shear strain, x is the depth from surface, y_0, and A and R are parameters.

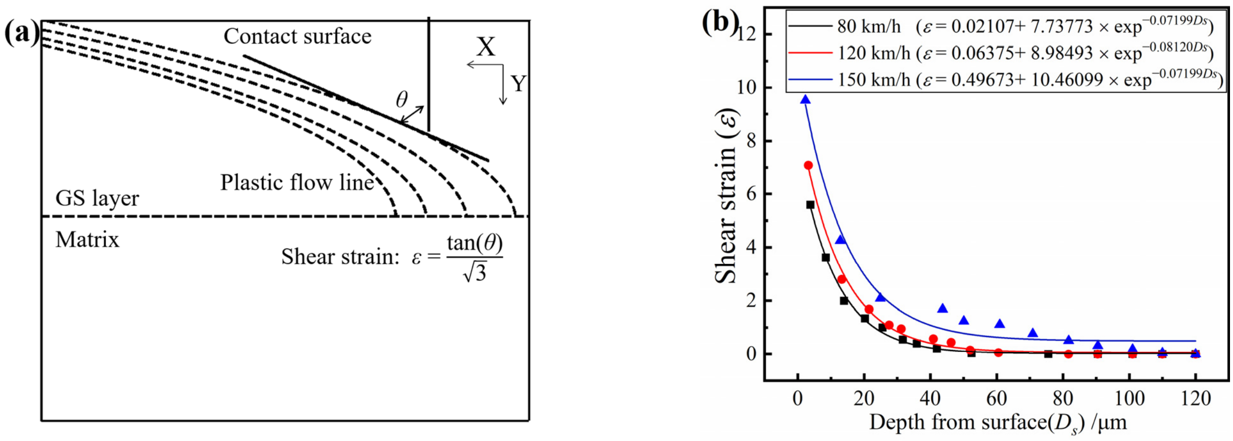

Figure 8. (**a**) Schematic of the shear strain and (**b**) curves of shear strain along with the depth.

According to Equations (5) and (6), the distribution of the shear strain along the depth from the surface (D_s) under different rotational speed conditions can be given in Figure 8b. It can be found that the shear stain (ε) and depth (Ds) of the plastic flow line displacement field satisfy the exponential relationship. As the D_s increases, the shear strain decreased monotonically at the surface and it finally tended to 0 in the matrix. Compared to 80 km/h, the shear strain increased significantly at 150 km/h.

The hardening of the wheel specimens was analyzed using microhardness. The hardness distribution of the gradient strain layer is shown in Figure 9, which also satisfy the exponential relationship according to the Equation (6). The hardness of the specimen profile was distributed in a gradient, which was similar to the shear strain curve (Figure 8b). Furthermore, the hardening rate of the GS layer was ~1.08 times higher at high running speeds (150 km/h) than at low running speeds (80 km/h).

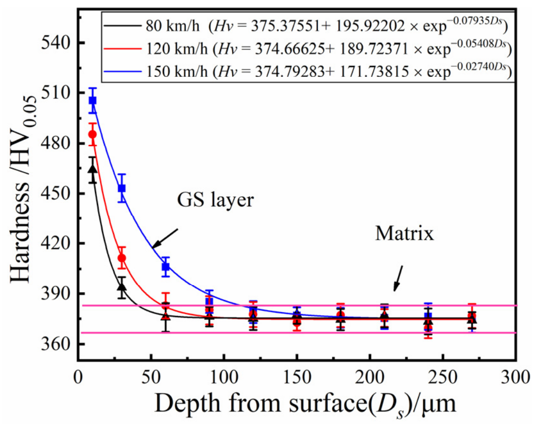

Figure 9. Curves of the distribution of hardness.

3.5. Fatigue Cracks Damage

When there is an inhomogeneous plastic deformation locally on the material surface, the ratcheting effect occurs as the plastic deformation accumulates, eventually leading to crack sprouting [45–47]. As can be seen above, as the running speed increases, the thickness of the GS layer on the surface of material and the degree of accumulation of plastic deformation gradually increased [48]. Figure 10 shows the fatigue cracking of the specimens at different running speeds. When the accumulation of plastic deformation reaches its limit, fatigue cracks start to appear on the surface or subsurface of material, forming a variety of cracks, such as main cracks, multilayer cracks, subsurface cracks, and branching cracks, and propagating along the matrix in the direction of plastic deformation [49]. However, these cracks do not always increase in size due to the amount of deformation and the crack driving force [50]. Branching cracks arose at the base of the main crack and propagate along the ferrite line parallel at an angle of deviation. Additionally, the materials above the cracked prevented the internal cracked materials from contacting the counter-frictional substrate, but they were easily crushed and broken under cyclic load (Figure 10(c1)).

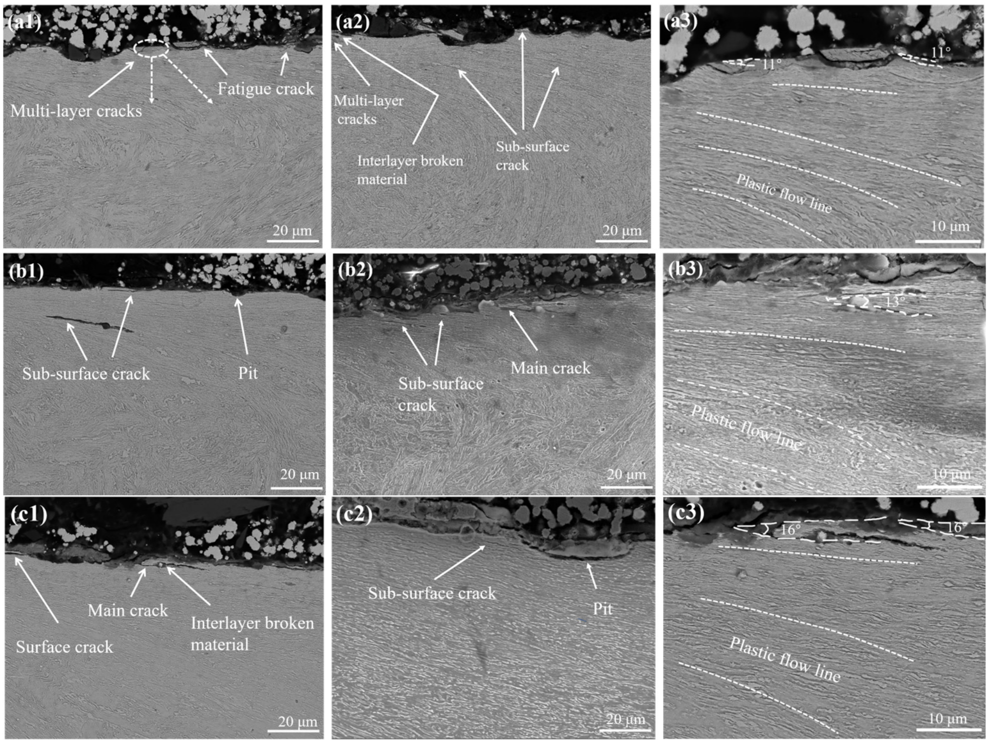

Figure 10. FESEM images of the fatigue cracks on the surface of the test steel: (**a1**–**a3**) 80 km/h, (**b1**–**b3**) 120 km/h and (**c1**–**c3**) 150 km/h.

4. Discussion

With the running speed increasing from 80 km/h to 150 km/h, the thickness of the GS layer (T_{GS}) increases from 42 to 110 μm and the hardening rate from 1.24 to 1.35, as shown in Figure 11. To provide insight into the wear-resistance of rolling-sliding wear of the novel BW presented in this study, alongside some representative wheel steel reported in previous studies (Table 5) [15,25,51,52]. The specific wear rate of the test steel was 1.01 (80 km/h), 0.88 (80 km/h) and 0.85 (80 km/h), which was one of the lowest compared to the pearlitic wheel (Figure 12). Additionally, opposite to the pearlitic wheel [15], the wear rate of the novel bainite wheel declines with the increase in running speed. It is well known that wear loss is a crucial parameter measuring the wear-resistance properties of wheel/rail materials [20,22,25].

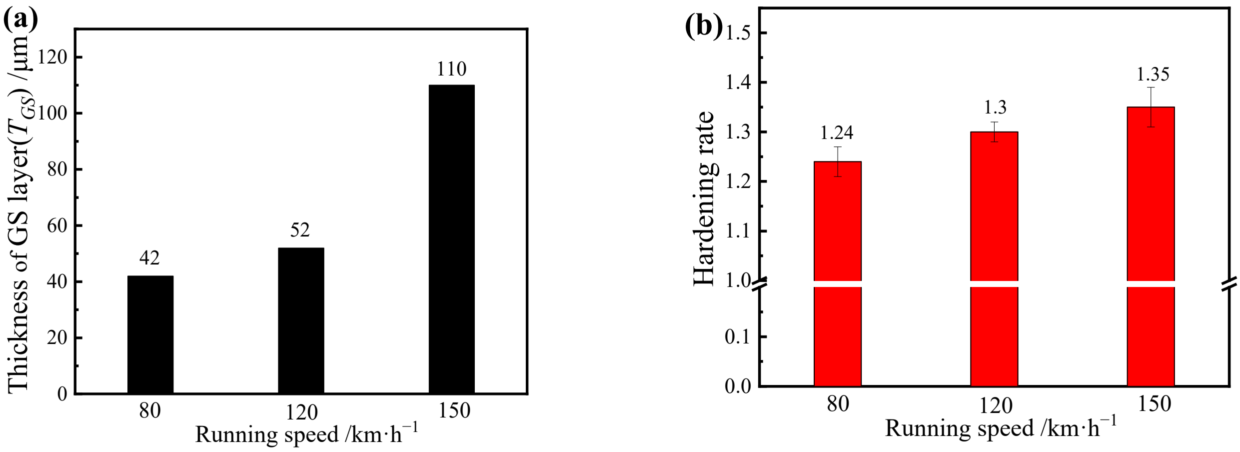

Figure 11. (**a**) The thickness of GS layer (T_{GS}) and (**b**) the hardening rate along with the running speeds.

Table 5. SWR data and chemical composition (wt%) of wear-resistant materials for railway reported under rolling–sliding wear.

Material	C	Si	Mn	Cr	Mo	V	SWR/mm^3·m^{-1}·N^{-1}	Ref.
Test steel	0.22~0.24	1.53~1.55	2.04~2.06	0.04~0.06	0.34~0.36	0.06~0.08	1.01×10^{-5}	Present work
PW-1	≤0.60	≤40	≤0.80	-	-	-	3.32×10^{-5}	[15]
PW-2	0.71	0.43	0.84	0.27	-	-	1.36×10^{-5}	[25]
ER7	≤0.48	≤0.40	≤0.75	-	-	-	1.95×10^{-5}	[51]
CL60	0.55~0.65	0.17~0.37	0.50~0.80	-	-	-	1.67×10^{-5}	[51]
B-Wheel	0.71	0.43	0.84	0.27	-	-	1.09×10^{-5}	[25]

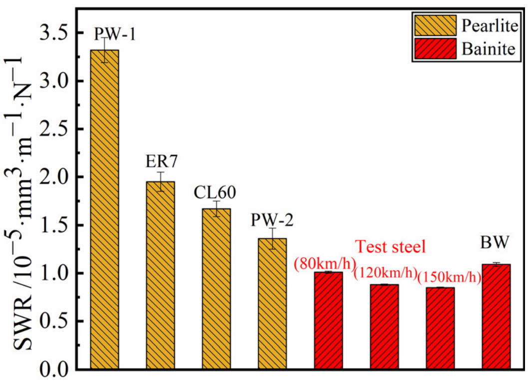

Figure 12. The comparison of the wear-resistance of the test steel and reported representative wheel material.

Previous studies have shown that the grain refinement due to the plastic deformation can improve the mechanical properties of materials according to the Hall-Petch strengthening mechanism [53]. In this study, the strengthening hardness of the gradient strain layer can be analyzed according to the classic Hall-Petch relation [54]:

$$\sigma = \sigma_0 + Kd^{-1/2} \tag{7}$$

where σ is the yield strength, σ_0 is material constant, K is the Hall-Petch coefficient, and d is the grain size of prior austenite.

With the formation of the gradient strain layer of wheel specimens, the grade of plastic deformation of bainite decreased gradually from surface to matrix. The grain was refined due to the SPD. The refinement of bainitic is the essential reason for the strengthening of microhardness, according to Equation (7). As the running speed increased, the shear stress [55] and strain of the GS layer were enhanced. The higher thickness and hardening were produced on the GS layer under higher running speed (Figure 11), which leads to the improvement of the wear resistance of the novel bainitic wheel steel. The information of specific wear rates could provide a guide in choosing bainitic wheel steel for the railway.

A relationship between the crack propagation depth and the crack propagation angle with the running speed is shown in Figure 13. The crack propagation angle and depth were at a minimum of ~11.4° and ~1.1 μm, respectively at 80 km/h, where the end of the crack appeared to buckle upwards. The crack was relatively small and was easy to spall. As the speed increases to 120 km/h, the crack propagation angle and crack propagation depth increase to ~13.1° and ~1.5 μm. At 150 km/h, the crack propagation angle and depth of crack propagation were at a maximum of ~16.8° and ~4.2 μm, respectively, where wear and fatigue damage were both particularly severe. If further expansion occurs, a fatigue fracture will occur, leading to the peeling of the wheel surface material. Thus, as the speed increases, the RCF cracks propagate along the line of plastic deformation, which leads to a gradual increase in the crack propagation depth and the crack propagation angle. When subjected to continued alternating stresses, the cracks propagated into the interior of the material, resulting in severe fatigue damage to the wheel.

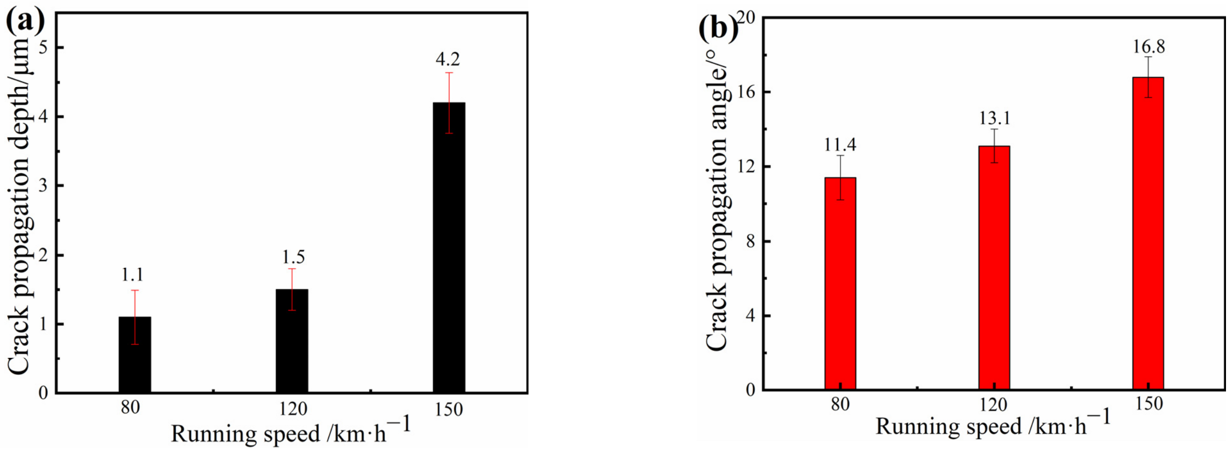

Figure 13. Curves of (**a**) the crack propagation depth and (**b**) the crack propagation angle with running speeds.

Normally, the wear has connected with the RCF damage. In the rolling-sliding wear tests, the wear was indicated by the mass losses of specimens, while the RCF damage was characterized by the cracks in the surface layer. In addition, the fracture of fatigue cracks would lead to the formation of wear debris, which could eventually result in material loss. Peeling due to fatigue is one of the forms of wear [56]. Thus, RCF damage can lead to wear. In a rolling-sliding wear test at a low running speed, the main wear mechanism was adhesion wear on the surface of the wheel with a small number of pits. As the speed increases, the density of cracks gradually decreases, but the length increases. The fatigue damage increases as the speed increases and adhesion wear cannot effectively eliminate cracks [57].

5. Conclusions

In this work, a novel bainitic wheel steel with a superior rolling-sliding wear-resistance was designed and prepared. The following main conclusions can be drawn:

(1) The novel bainitic wheel steel consists of carbide-free bainite and film-like retained austenite and exhibited outstanding mechanical properties with a high yield strength of 950 MPa and a hardness of 415 HV, which were superior to those of most of the reported typical pearlitic wheel steel.

(2) During the process of wear, the surface damage of the wheel was mainly adhesive wear and fatigue damage, and the gradient strain layer (GS layer) was formed on

the wheel surface. With the increasing running speed, the fatigue cracks on wheel specimens were more serious and adhesive wear lightens, and the surface morphology of the wheel turned from pitting pits to peeling.

(3) As the running speed increased, the shear stress and strain of the GS layer were enhanced. The higher thickness and hardening were produced on the GS layer under higher running speed, which led to the improvement of the wear resistance of the novel bainitic wheel steel. This is the main reason for the wear rate of the bainite wheel decreasing with increasing running speed.

(4) The novel bainitic wheel steel exhibited an excellent wear-resistance after rolling-sliding wear, which was much better than that of most of the reported representative pearlitic wheel steel. Thus, the novel bainitic wheel is a very promising wheel material for heavy-haul railway applications.

Author Contributions: Methodology and supervision, Y.H.; project administration, Y.H. and T.Z.; writing—original draft, T.Z. and H.X.; investigation, Z.X. and H.Z.; data curation, X.M. All authors have read and agreed to the published version of the manuscript.

Funding: This research was funded by Major Consulting Project of Chinese Academy of Engineering (No. ZGZ201812-03) and Key Project of Science and Technology in Anhui Province (No. 202003a05020038).

Data Availability Statement: All data that support the findings of this study are included within the article.

Acknowledgments: The authors thank Shihong Wang of Central Iron and Steel Research Institute for using JMat-Pro software for thermodynamic simulation.

Conflicts of Interest: The authors declare no conflict of interest.

References

1. Zhang, R.J.; Zheng, C.L.; Lv, B.; Zhang, P.J.; Gao, G.H.; Yang, Y.Q.; Zhang, F.C. Effect of non-uniform microstructure on rolling contact fatigue performance of bainitic rail steel. *Int. J. Fatigue* **2022**, *159*, 106795. [CrossRef]
2. Strey, N.F.; Rezende, A.B.; Miranda, R.D.; da Fonseca, S.T.; Mei, P.R.; Scandian, C. Comparison of rolling contact fatigue damage between railway wheels and twin-disc test specimens. *Tribol. Int.* **2021**, *160*, 107037. [CrossRef]
3. Seo, J.W.; Hur, H.M.; Kwon, S.J. Effect of Mechanical Properties of Rail and Wheel on Wear and Rolling Contact Fatigue. *Metals* **2022**, *12*, 630. [CrossRef]
4. Song, J.D.; Shi, L.B.; Ding, H.H.; Galas, R.; Omasta, M.; Wang, W.J.; Guo, J.; Liu, Q.Y.; Hartl, M. Effects of solid friction modifier on friction and rolling contact fatigue damage of wheel-rail surfaces. *Friction* **2022**, *10*, 597–607. [CrossRef]
5. Yu, F.; Lin, F.; Tang, Y.; Zhong, C. High-speed railway to success? The effects of high-speed rail connection on regional economic development in China. *J. Reg. Sci.* **2019**, *59*, 723–742. [CrossRef]
6. Jin, X.S. Research Progress of High-Speed Wheel-Rail Relationship. *Lubricants* **2022**, *10*, 248. [CrossRef]
7. Bai, W.; Zhou, L.; Wang, P.F.; Hu, Y.; Wang, W.J.; Ding, H.H.; Han, Z.Y.; Xu, X.J.; Zhu, M.H. Damage behavior of heavy-haul rail steels used from the mild conditions to harsh conditions. *Wear* **2022**, *496*, 204290. [CrossRef]
8. Guo, L.C.; Zhu, W.T.; Shi, L.B.; Liu, Q.Y.; Cai, Z.B.; Wang, W.J. Study on wear transition mechanism and wear map of CL60 wheel material under dry and wet conditions. *Wear* **2019**, *426*, 1771–1780. [CrossRef]
9. Liu, C.P.; Liu, P.T.; Pan, J.Z.; Chen, C.H.; Ren, R.M. Effect of pre-wear on the rolling contact fatigue property of D2 wheel steel. *Wear* **2020**, *442*, 203154. [CrossRef]
10. Faccoli, M.; Petrogalli, C.; Lancini, M.; Ghidini, A.; Mazzu, A. Effect of desert sand on wear and rolling contact fatigue behaviour of various railway wheel steels. *Wear* **2018**, *396*, 146–161. [CrossRef]
11. Leso, T.P.; Siyasiya, C.W.; Mostert, R.J.; Moema, J. Study of rolling contact fatigue, rolling and sliding wear of class B wheel steels against R350HT and R260 rail steels under dry contact conditions using the twin disc setup. *Tribol. Int.* **2022**, *174*, 107711. [CrossRef]
12. Liu, C.P.; Zhao, X.J.; Liu, P.T.; Pan, J.Z.; Ren, R.M. Influence of Rotational Speed on Subsurface Microstructure and Wear Property of D2/U71Mn Wheel-Rail Steel. *Tribol. Trans.* **2022**, *65*, 1059–1068. [CrossRef]
13. Seo, J.W.; Kwon, S.J.; Jun, H.K.; Lee, C.W. Effects of Wheel Materials on Wear and Fatigue Damage Behaviors of Wheels/Rails. *Tribol. Trans.* **2019**, *62*, 635–649. [CrossRef]
14. Hua, J.; Liu, P.T.; Pan, J.Z.; Zhang, G.N.; Wu, S.; Su, C.; Zhao, X.J.; Ren, R.M. Study on the effect of rotational speed on the polygonisation formation mechanism, microstructure and property evolution of D2 wheel steel. *Wear* **2021**, *484*, 204044. [CrossRef]
15. Ding, H.H.; Fu, Z.K.; Wang, W.J.; Guo, J.; Liu, Q.Y.; Zhu, M.H. Investigation on the effect of rotational speed on rolling wear and damage behaviors of wheel/rail materials. *Wear* **2015**, *330*, 563–570. [CrossRef]
16. Chen, S.Y.; Liu, J.H.; Guo, J.; Wang, W.J.; Liu, Q.Y. Effect of wheel material characteristics on wear and fatigue property of wheel-rail. *Tribology* **2015**, *35*, 531–537. [CrossRef]

17. Li, G.; Hong, Z.Y.; Yan, Q.Z. The influence of microstructure on the rolling contact fatigue of steel for high-speed-train wheel. *Wear* **2015**, *342*, 349–355. [CrossRef]
18. Zhang, G.Z.; Liu, C.P.; Ren, R.M.; Wu, S.; Yin, H.X.; Cong, T.; Li, X. Effect of nonuniform microstructure on wear property of ER8 wheel steel. *Wear* **2020**, *458*, 203416. [CrossRef]
19. Liu, J.P.; Li, Y.Q.; Zhou, Q.Y.; Zhang, Y.H.; Hu, Y.; Shi, L.B.; Wang, W.J.; Liu, F.S.; Zhou, S.B.; Tian, C.H. New insight into the dry rolling-sliding wear mechanism of carbide-free bainitic and pearlitic steel. *Wear* **2019**, *432*, 202943. [CrossRef]
20. Hasan, S.M.; Chakrabarti, D.; Singh, S.B. Dry rolling/sliding wear behaviour of pearlitic rail and newly developed carbide-free bainitic rail steels. *Wear* **2018**, *408*, 151–159. [CrossRef]
21. Sharma, S.; Sangal, S.; Mondal, K. Wear behaviour of bainitic rail and wheel steels. *Mater. Sci. Technol.* **2016**, *32*, 266–274. [CrossRef]
22. Rezende, A.B.; Fonseca, S.T.; Fernandes, F.M.; Miranda, R.S.; Grijalba, F.A.F.; Farina, P.F.S.; Mei, P.R. Wear behavior of bainitic and pearlitic microstructures from microalloyed railway wheel steel. *Wear* **2020**, *456*, 203377. [CrossRef]
23. Miranda, R.S.; Rezende, A.B.; Fonseca, S.T.; Fernandes, F.M.; Sinatora, A.; Mei, P.R. Fatigue and wear behavior of pearlitic and bainitic microstructures with the same chemical composition and hardness using twin-disc tests. *Wear* **2022**, *494–495*, 204253. [CrossRef]
24. Krolicka, A.; Lesiuk, G.; Radwa, K.; Kuziak, R.; Janik, A.; Mech, R.; Zygmunt, T. Comparison of fatigue crack growth rate: Pearlitic rail versus bainitic rail. *Int. J. Fatigue* **2021**, *149*, 106280. [CrossRef]
25. Hu, Y.; Guo, L.C.; Maiorino, M.; Liu, J.P.; Ding, H.H.; Lewis, R.; Meli, E.; Rindi, A.; Liu, Q.Y.; Wang, W.J. Comparison of wear and rolling contact fatigue behaviours of bainitic and pearlitic rails under various rolling-sliding conditions. *Wear* **2020**, *460*. [CrossRef]
26. Liu, M.; Fan, Y.S.; Gui, X.L.; Hu, J.; Wang, X.; Gao, G.H. Relationship between Microstructure and Properties of 1380 MPa Grade Bainitic Rail Steel Treated by Online Bainite-Based Quenching and Partitioning Concept. *Metals* **2022**, *12*, 330. [CrossRef]
27. Das Bakshi, S.; Leiro, A.; Prakash, B.; Bhadeshia, H.K.D.H. Dry rolling/sliding wear of nanostructured bainite. *Wear* **2014**, *316*, 70–78. [CrossRef]
28. Fan, Y.; Gui, X.; Liu, M.; Wang, X.; Bai, B.; Gao, G. Effect of microstructure on wear and rolling contact fatigue behaviors of bainitic/martensitic rail steels. *Wear* **2022**, *508–509*, 204474. [CrossRef]
29. Valizadeh Moghaddam, P.; Hardell, J.; Vuorinen, E.; Prakash, B. Dry sliding wear of nanostructured carbide-free bainitic steels—Effect of oxidation-dominated wear. *Wear* **2020**, *454–455*, 203317. [CrossRef]
30. Kumar, A.; Dutta, A.; Makineni, S.K.; Herbig, M.; Petrov, R.H.; Sietsma, J. In-situ observation of strain partitioning and damage development in continuously cooled carbide-free bainitic steels using micro digital image correlation. *Mater. Sci. Eng. A* **2019**, *757*, 107–116. [CrossRef]
31. Caballero, F.G.; Allain, S.; Cornide, J.; Puerta Velásquez, J.D.; Garcia-Mateo, C.; Miller, M.K. Design of cold rolled and continuous annealed carbide-free bainitic steels for automotive application. *Mater. Des.* **2013**, *49*, 667–680. [CrossRef]
32. Xu, X.; Wang, Z.; Gao, G.; Zhang, X.; Kang, G.; Kan, Q. The effect of microstructure evolution on the ratchetting-fatigue interaction of carbide-free bainite rail steels under different heat-treatment conditions. *Int. J. Fatigue* **2022**, *160*, 106872. [CrossRef]
33. Shipway, P.H.; Wood, S.J.; Dent, A.H. The hardness and sliding wear behaviour of a bainitic steel. *Wear* **1997**, *203–204*, 196–205. [CrossRef]
34. *GB/T. GB/T8601-2021*; Forged and Rolled Solid Wheels for Railway. Metallurgical Industry Press: Beijing, China, 2021; pp. 1–32.
35. Bodini, I.; Petrogalli, C.; Faccoli, M.; Mazzu, A. Vision-based damage analysis in shoe-braking tests on railway wheel steels. *Wear* **2022**, *510*, 204514. [CrossRef]
36. Xin, Y.; Zhao, X.J.; Pan, J.Z.; Pan, R.; Ren, R.M. Influences of Microstructure on Sliding Wear Performance of D2 Wheel Steel. *Tribology* **2019**, *39*, 479. [CrossRef]
37. Zeng, D.F.; Xu, T.; Liu, W.D.; Lu, L.T.; Zhang, J.W.; Gong, Y.H. Investigation on rolling contact fatigue of railway wheel steel with surface defect. *Wear* **2020**, *446*, 203207. [CrossRef]
38. Yang, L.; Zhou, T.; Xu, Z.; He, Y.; Hu, X.; Zhao, H. Excellent Wear Resistance of a High-Speed Train Brake Disc Steel with High Hardening Ratcheting Strain Zone. *Metals* **2021**, *11*, 1478. [CrossRef]
39. *YB/T. YB/T5345-2014*; Rolling Contact Fatigue Test Method for Metal Materials. Metallurgical Industry Press: Beijing, China, 2014; pp. 1–23.
40. Hardwick, C.; Lewis, R.; Eadie, D.T. Wheel and rail wear-Understanding the effects of water and grease. *Wear* **2014**, *314*, 198–204. [CrossRef]
41. Leiro, A.; Vuorinen, E.; Sundin, K.G.; Prakash, B.; Sourmail, T.; Smanio, V.; Caballero, F.G.; Garcia-Mateo, C.; Elvira, R. Wear of nano-structured carbide-free bainitic steels under dry rolling-sliding conditions. *Wear* **2013**, *298*, 42–47. [CrossRef]
42. Liu, Y.X.; Chen, H.; Wang, R.Z.; Jia, Y.F.; Zhang, X.C.; Cui, Y.; Tu, S.T. Fatigue behaviors of 2205 duplex stainless steel with gradient nanostructured surface layer. *Int. J. Fatigue* **2021**, *147*, 106170. [CrossRef]
43. An, L.; Sun, Y.-T.; Lu, S.-P.; Wang, Z.-B. Enhanced Fatigue Property of Welded S355J2W Steel by Forming a Gradient Nanostructured Surface Layer. *Acta Metall. Sin. (Engl. Lett.)* **2020**, *33*, 1252–1258. [CrossRef]
44. Widiyarta, I.M.; Franklin, F.J.; Kapoor, A. Modelling thermal effects in ratcheting-led wear and rolling contact fatigue. *Wear* **2008**, *265*, 1325–1331. [CrossRef]
45. Tyfour, W.R.; Beynon, J.H. The effect of rolling direction reversal on the wear rate and wear mechanism of pearlitic rail steel. *Tribol. Int.* **1994**, *27*, 401–412. [CrossRef]
46. Vishnuvardhan, S.; Raghava, G.; Gandhi, P.; Saravanan, M.; Goyal, S.; Arora, P.; Gupta, S.K.; Bhasin, V. Ratcheting failure of pressurised straight pipes and elbows under reversed bending. *Int. J. Press. Vessel. Pip.* **2013**, *105*, 79–89. [CrossRef]
47. Tyfour, W.R.; Beynon, J.H.; Kapoor, A. Deterioration of rolling contact fatigue life of pearlitic rail steel due to dry-wet rolling-sliding line contact. *Wear* **1996**, *197*, 255–265. [CrossRef]

48. Su, X.; Clayton, P. Ratchetting strain experiments with a pearlitic steel under rolling/sliding contact. *Wear* **1997**, *205*, 137–143. [CrossRef]
49. Oliveira, M.C.; Alves, J.L.; Chaparro, B.M.; Menezes, L.F. Study on the influence of work-hardening modeling in springback prediction. *Int. J. Plast.* **2007**, *23*, 516–543. [CrossRef]
50. Rycerz, P.; Olver, A.; Kadiric, A. Propagation of surface initiated rolling contact fatigue cracks in bearing steel. *Int. J. Fatigue* **2017**, *97*, 29–38. [CrossRef]
51. Hu, Y.; Zhou, L.; Ding, H.H.; Tan, G.X.; Lewis, R.; Liu, Q.Y.; Guo, J.; Wang, W.J. Investigation on wear and rolling contact fatigue of wheel-rail materials under various wheel/rail hardness ratio and creepage conditions. *Tribol. Int.* **2020**, *143*, 106091. [CrossRef]
52. Rong, K.-J.; Xiao, Y.-L.; Shen, M.-X.; Zhao, H.-P.; Wang, W.-J.; Xiong, G.-Y. Influence of ambient humidity on the adhesion and damage behavior of wheel–rail interface under hot weather condition. *Wear* **2021**, *486–487*, 204091. [CrossRef]
53. Wu, B.B.; Wang, X.L.; Wang, Z.Q.; Zhao, J.X.; Jin, Y.H.; Wang, C.S.; Shang, C.J.; Misra, R.D.K. New insights from crystallography into the effect of refining prior austenite grain size on transformation phenomenon and consequent mechanical properties of ultra-high strength low alloy steel. *Mater. Sci. Eng. A* **2019**, *745*, 126–136. [CrossRef]
54. Hall, E. Variation of hardness of metals with grain size. *Nature* **1954**, *173*, 948–949. [CrossRef]
55. Ghatrehsamani, S.; Akbarzadeh, S.; Khonsari, M.M. Relationship between subsurface stress and wear particle size in sliding contacts during running-in. *Mech. Res. Commun.* **2022**, *123*, 103891. [CrossRef]
56. Ma, L.; He, C.G.; Zhao, X.J.; Guo, J.; Zhu, Y.; Wang, W.J.; Liu, Q.Y.; Jin, X.S. Study on wear and rolling contact fatigue behaviors of wheel/rail materials under different slip ratio conditions. *Wear* **2016**, *366–367*, 13–26. [CrossRef]
57. Ueda, M.; Matsuda, K. Effects of carbon content and hardness on rolling contact fatigue resistance in heavily loaded pearlitic rail steels. *Wear* **2020**, *444*, 203120. [CrossRef]

Disclaimer/Publisher's Note: The statements, opinions and data contained in all publications are solely those of the individual author(s) and contributor(s) and not of MDPI and/or the editor(s). MDPI and/or the editor(s) disclaim responsibility for any injury to people or property resulting from any ideas, methods, instructions or products referred to in the content.